

Teeth Localization and Lesion Segmentation in CBCT Images using SpatialConfiguration-Net and U-Net

Arnela Hadzic¹, Barbara Kirnbauer², Darko Štern³ and Martin Urschler¹

¹*Institute for Medical Informatics, Statistics and Documentation, Medical University of Graz, Graz, Austria*

²*Department of Dental Medicine and Oral Health, Medical University of Graz, Graz, Austria*

³*Institute of Computer Graphics and Vision, Graz University of Technology, Graz, Austria*

Keywords: Teeth Localization, Lesion Segmentation, SpatialConfiguration-Net, U-Net, CBCT, Class Imbalance

Abstract: The localization of teeth and segmentation of periapical lesions in cone-beam computed tomography (CBCT) images are crucial tasks for clinical diagnosis and treatment planning, which are often time-consuming and require a high level of expertise. However, automating these tasks is challenging due to variations in shape, size, and orientation of lesions, as well as similar topologies among teeth. Moreover, the small volumes occupied by lesions in CBCT images pose a class imbalance problem that needs to be addressed. In this study, we propose a deep learning-based method utilizing two convolutional neural networks: the SpatialConfiguration-Net (SCN) and a modified version of the U-Net. The SCN accurately predicts the coordinates of all teeth present in an image, enabling precise cropping of teeth volumes that are then fed into the U-Net which detects lesions via segmentation. To address class imbalance, we compare the performance of three reweighting loss functions. After evaluation on 144 CBCT images, our method achieves a 97.3% accuracy for teeth localization, along with a promising sensitivity and specificity of 0.97 and 0.88, respectively, for subsequent lesion detection.

1 INTRODUCTION

Cone-beam computed tomography (CBCT) is a highly effective medical imaging technique used to generate a 3D image of the oral and maxillofacial region, with various applications in dentistry (Khanagar et al., 2021; Umer and Habib, 2022). However, the analysis and documentation of CBCT images typically require a significant amount of time and expertise from professionals. While automated methods have been proposed to localize and segment anatomical structures in general medical images, this remains challenging for dental structures due to the presence of similar topologies and appearances among teeth, unclear boundaries, artifacts, or variations in shapes, appearance and size of lesions. Moreover, in dental images lesions occupy a significantly smaller volume compared to the background and they only affect a small percentage of teeth in patients, resulting in class imbalance which poses another major challenge.

Early approaches for localizing anatomical structures in medical images were based on statistical models of shape and appearance (Cootes et al., 1994), which were later improved by incorporating random forest-based machine learning models (Donner et al., 2013; Unterpinker et al., 2015; Urschler et al., 2018). Recently, deep learning-based methods have outper-

formed traditional machine learning localization approaches in terms of accuracy and efficiency. (Zhang et al., 2017) proposed two deep convolutional neural networks (CNNs) for detecting anatomical landmarks in brain MR volumes, where the first network captures inherent relationships between local image patches and target landmarks, while the second network predicts landmark coordinates directly from the input image. (Jain et al., 2014) found that regressing heatmaps rather than coordinates improves the overall performance of landmark detection and also simplifies the analysis of network’s predictions. Building on this idea, (Payer et al., 2019) proposed the SpatialConfiguration-Net, which combines local appearance responses with the spatial configuration of landmarks in an end-to-end manner and achieved state-of-the-art performance on a variety of medical datasets. Regarding teeth detection in CBCT images, several studies that use CNNs have been published. (Chung et al., 2020) adopted a faster R-CNN framework to localize individual tooth regions inside volume of interest regions, which were previously extracted and realigned using a 2D pose regression CNN. More recently, (Du et al., 2022) employed a classification network to extract tooth regions and trained a YOLOv3 network to detect teeth bounding boxes within these regions.

Early approaches for segmenting structures in medical images often relied on active contours or statistical shape models (Heimann and Meinzer, 2009; Gan et al., 2017). Their limitation of requiring pre-defined handcrafted features was recently overcome by deep learning-based methods. To date, several research studies have been proposed for the automated detection of periapical lesions in dental images using deep learning. Most of these studies focus on periapical or panoramic radiographs (Ekert et al., 2019; Endres et al., 2020; Krois et al., 2021; Pauwels et al., 2021), which exhibit lower accuracy compared to using CBCT scans (Antony et al., 2020), potentially leading to missed or hidden lesions. To the best of our knowledge, only a limited number of research studies have addressed the automated detection or segmentation of periapical lesions in CBCT images. (Lee et al., 2020) employed a CNN architecture based on the GoogLeNet Inception v3 model and trained it on cropped 2D slices from CBCT images. They achieved a sensitivity value of 0.94 for periapical lesion detection. (Setzer et al., 2020) used a U-Net-based architecture to segment periapical lesions in limited field-of-view CBCT data. Their model achieved a sensitivity of 0.93 and a specificity of 0.88, with an average Dice score of 0.52 for all positive examples and 0.67 for true positive examples. However, their training and testing involved 2D scans from only 20 CBCT volumes with 61 roots. In another study, (Zheng et al., 2020) trained an anatomically constrained Dense U-Net using 2D slices from 20 CBCT images. They incorporated oral-anatomical knowledge that periapical lesions are located near the roots of teeth and achieved a sensitivity value of 0.84. (Orhan et al., 2020) employed two separate U-Net-like CNN architectures for teeth localization and periapical lesion segmentation in CBCT images. The first network localized each tooth, and the second network used the extracted teeth with their context to detect lesions. However, the authors did not provide details about the architecture or the training/testing procedure of their networks. They reported detecting 142 out of 153 lesions correctly, resulting in a sensitivity of 92.8% for lesion detection, with only one misidentified tooth. They did not provide an evaluation of negative examples, nor did they clarify whether 3D volumes were used throughout their method.

Although deep learning techniques have demonstrated potential in automating the detection of periapical lesions in CBCT images, current methods often rely on training procedures based solely on 2D slices, which may result in the loss of valuable information. To address this concern, it is important to incorporate 3D volumes into the training process to

effectively utilize all available data. Additionally, the issue of class imbalance should be taken into account, since lesions occupy only small volumes in images, and the majority of teeth are lesion-free.

In this work, we have developed a fully automated deep learning method for the detection of teeth and periapical lesions in 3D CBCT images in a multi-step process. First, we use the 3D SpatialConfigurationNet to perform the teeth localization, i.e., to generate a 3D coordinate of each tooth in an image. Then, we automatically crop each tooth in the image based on the generated coordinates. Finally, we train a 3D U-Net using the previously cropped volumes to segment periapical lesions. To address the commonly encountered class imbalance problem in medical datasets, we use and compare three different reweighting loss functions during both the training and testing procedures. Utilization of state-of-the-art (SOTA) 3D network architectures for respective tasks as well as adaptation to address class imbalance problems contribute to the reliability and high accuracy of our method. The objective of this study is to provide a comprehensive description of the techniques used to obtain the results that we recently published in a clinical journal (Kirnbauer et al., 2022), and to shed light on the significant issues of class imbalance and preservation of 3D volumetric information.

2 METHOD

2.1 Data

Our method was trained and tested on a dataset that consists of 144 3D CBCT images provided by the University Clinic for Dentistry and Oral Health Graz. Ethical approval was granted by the Medical University of Graz under review board number 33-048 ex 20/21. Out of the 144 images, 16 images visualize both jaws, while the remaining 128 images visualize either the upper or lower jaw. The images visualize 2128 teeth, and in most images at least one periapical lesion was found. In total, approximately 10% of the teeth in the dataset were affected by a periapical lesion, thus leading to class imbalance.

To obtain ground truth data, we first perform a manual localization of each tooth location, thus creating a set of 32 coordinates for each image. If a tooth is missing, we annotate it with the coordinate $(-1, -1, -1)$. Second, for the ground truth segmentation of periapical lesions in an image, we use the semi-automatic Total Variation (TV) framework proposed in (Urschler et al., 2014). Each lesion segmentation was then verified by an experienced dentist us-

ing the ITK-Snap software (Yushkevich et al., 2006) and manually adjusted if necessary.

2.2 CNN Architecture

The developed method consists of two networks (see Figs. 1 and 2): the SpatialConfiguration-Net (Payer et al., 2019), and a modified version of the U-Net (Ronneberger et al., 2015). The method includes an additional cropping step in between, a design inspired by (Payer et al., 2020).

2.2.1 Teeth Localization

As the first step towards the detection of periapical lesions in 3D CBCT images, we perform the teeth localization using the SpatialConfiguration-Net (SCN). SCN is a fully convolutional neural network that consists of two main components: *local appearance* (LA) and *spatial configuration* (SC). The LA component generates locally accurate predictions, but they may be ambiguous. To solve this issue, the SC component incorporates the spatial relationship between landmarks into the network.

The network is trained to produce heatmap images of landmarks, where each heatmap image represents the probability of a specific landmark being present at a particular location in the image. The predicted coordinate x'_i of a landmark L_i , where $i \in \{1, \dots, 32\}$, is defined as the coordinate where the predicted heatmap $h_i(x; w, b)$ has its highest value.

For each image in our dataset, we create a target heatmap image g by merging Gaussian heatmaps of its ground truth landmarks. A Gaussian heatmap $g_i(x; \sigma_i)$ of a ground truth landmark L_i is defined by

$$g_i(x; \sigma_i) = \exp\left(-\frac{\|x - \tilde{x}_i\|_2^2}{2\sigma_i^2}\right), \quad (1)$$

where x are image coordinates and \tilde{x}_i is the ground truth coordinate of the landmark L_i . The heatmap peak widths are determined by the standard deviation σ and depend on the distance between the image coordinates and the ground truth coordinate. Higher values are assigned to voxels that are closer to the ground truth coordinate \tilde{x}_i , while the values of voxels further away from \tilde{x}_i decrease gradually.

To minimize differences between the predicted $h_i(x; w, b)$ and the target heatmaps $g_i(x; \sigma_i)$ for each landmark L_i , we minimize the objective function

$$\min_{w, b, \sigma} \sum_{i=0}^{N-1} \sum_x \|h_i(x; w, b) - g_i(x; \sigma_i)\|_2^2 \cdot M(x) + T, \quad (2)$$

where

$$T = \alpha \|\sigma\|_2^2 + \lambda \|w\|_2^2. \quad (3)$$

We calculate the distance between the predicted heatmaps and the target heatmaps using the L_2 measure, which is multiplied with a binary mask $M(x)$. When the ground truth annotation at location x is annotated as missing, the value of x in $M(x)$ is set to zero. This way, the network ignores the predictions for missing teeth. The heatmap peak widths $\sigma = (\sigma_0, \sigma_1, \dots, \sigma_{N-1})^T$, the network weights w , and the bias b are learnable parameters of the network. The factor α determines how strong the heatmap peak widths σ are being penalized, while λ determines the impact of the L_2 norm of the weights w .

The LA component consists of four levels, where each level includes three convolutional layers and one average pooling layer, except for the last level where downsampling is not performed. The SC component consists of one level with four $7 \times 7 \times 7$ convolutional layers, three of which have 64 outputs and one has 32 outputs. The inputs to the first convolutional layer are the local appearance heatmaps H_{LA} generated by the LA component, downsampled by a factor of 4. To generate the set of spatial configuration heatmaps H_{SC} , the 32 outputs of the last convolutional layer are upsampled to the input resolution using tricubic interpolation. All convolutional layers, except the ones generating H_{LA} and H_{SC} , have a LeakyReLU activation function with a negative slope of 0.1. The weights are initialized using the He initializer (He et al., 2015). The layer generating H_{LA} has a linear activation function, while the layer generating H_{SC} has a TanH activation function. Both layers initialize the biases with 0 and the weights using a Gaussian distribution with a standard deviation of 0.001. A dropout rate of 0.3 is applied after the first convolutional layer in each level.

As shown in Fig. 1, the LA and SC components generate separate heatmap images, which are then multiplied voxel-wise to generate the final output of the SCN. Using the coordinates predicted by the SCN, all teeth present in the images are cropped to the size of $[64, 64, 64]$ and fed into the U-Net for lesion segmentation.

2.2.2 Lesion Segmentation

For the segmentation of periapical lesions, we use a modified version of the U-Net. Our adaptation consists of 5 levels, where each convolutional layer has a kernel size of $[3, 3, 3]$ and 16 filter outputs. In the contracting path, we use convolutional operations followed by downsampling through average pooling. In the expansive path, each upsampling layer performs trilinear interpolation followed by two convolutional operations. After each convolutional layer we apply a dropout of 0.3, and use 'same' padding to maintain the

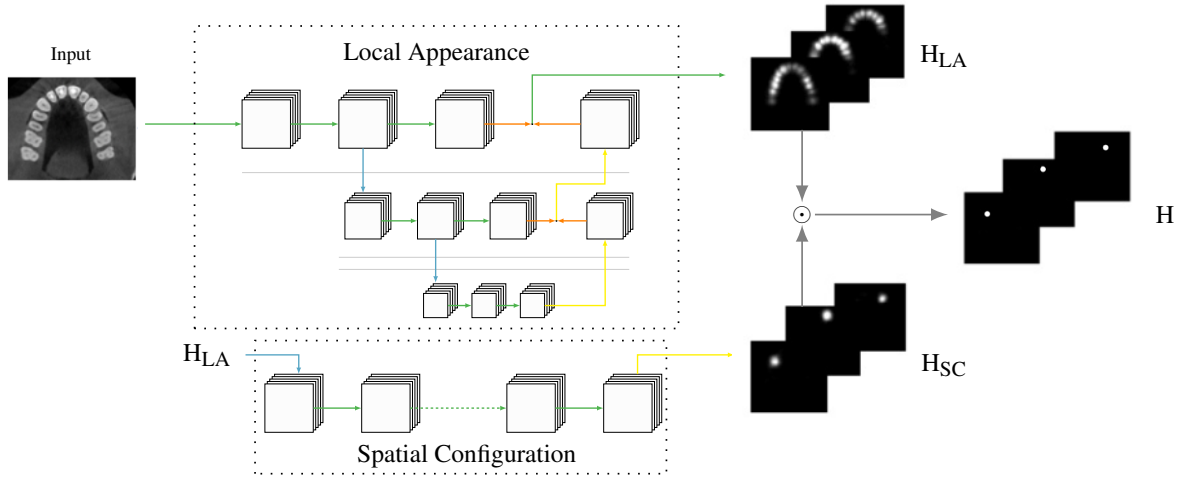


Figure 1: Teeth localization using SpatialConfiguration-Net. The local appearance component generates a set of local appearance heatmaps denoted as H_{LA} , while the spatial configuration component produces a set of spatial configuration heatmaps H_{SC} . The final heatmap images H for teeth landmarks are obtained by performing voxel-wise multiplication of H_{LA} and H_{SC} . The arrows represent different operations: green arrow – convolution, blue arrow – downsampling, yellow arrow – upsampling, and orange arrow – voxel-wise addition.

same input and output size. All layers have a ReLU activation function except the last one, where no activation function is used in order to obtain logits instead of probabilities as the network’s output. Same as for the SCN, the weights in the last layer are initialized with the He initializer. In all other layers, the initial weights are sampled from a truncated normal distribution with a standard deviation of 0.001. The last layer consists of a single output, generating an image with predicted intensity values. The network’s output is an image of size $[64, 64, 64]$, with voxel intensities in the range $(-\infty, +\infty)$. Finally, a threshold of 0 was applied to the output in order to produce the predicted binary segmentation map, where all voxel values below the threshold are considered background, while non-negative values represent a detected lesion.

To address the class imbalance problem, we compare three objective functions, Focal Loss FL (Lin et al., 2017), Focal Tversky Loss FTL (Abraham and Khan, 2019), and Combo Loss CL (Taghanaki et al., 2019) based on Dice Similarity Coefficient (DSC):

$$FL(p_t) = -\alpha_t(1 - p_t)^\gamma \log(p_t), \quad (4)$$

$$FTL(P, G) = (1 - TI(P, G))^{\frac{1}{\gamma}}, \quad (5)$$

and

$$CL(y, p) = \delta \cdot L_{BBCE}(y, p) - (1 - \delta) \cdot DSC(y, p). \quad (6)$$

In the above equations, Tversky Index (TI) and Balanced Binary Cross-Entropy (BBCE) are defined by

$$TI(P, G) = \frac{|PG| + \epsilon}{|PG| + \beta|P \setminus G| + (1 - \beta)|G \setminus P| + \epsilon} \quad (7)$$

and

$$L_{BBCE}(y, p) = -\alpha \cdot y \log(p) - (1 - \alpha) \cdot (1 - y) \log(1 - p). \quad (8)$$

The parameters α and β in the above equations are used to weight positive and negative examples. α can be set as the inverse class frequency or considered as a hyperparameter, while values of β larger than 0.5 give more significance to false negative examples. To enhance the focus on misclassified predictions, γ should be larger than 0 in the FL function and larger than 1 in the FTL function. The parameter δ regulates the contribution of the BBCE to the CL function.

2.3 Data Augmentation

To prepare images for training the SCN for localization, we resize all images from the original size of $[501, 501, 501]$ to a new size of $[64, 64, 32]$, while maintaining a fixed aspect ratio. As we do not need highly precise locations of teeth for the lesion segmentation task, the SCN can be trained on downsampled images. Image intensities are then scaled to the range $[-1, 1]$. Additionally, images undergo translation, rotation, and scaling using random factors sampled from uniform distributions ($[-10, 10]$ for translation, $[-0.1, 0.1]$ for rotation, $[0.9, 1.1]$ for scaling).

Before training our modified U-Net for the lesion segmentation task, original high-resolution images are cropped along with their corresponding ground truth segmentation maps for each tooth. This process generates 32 cropped images from a single original image, where the center of each cropped image corre-

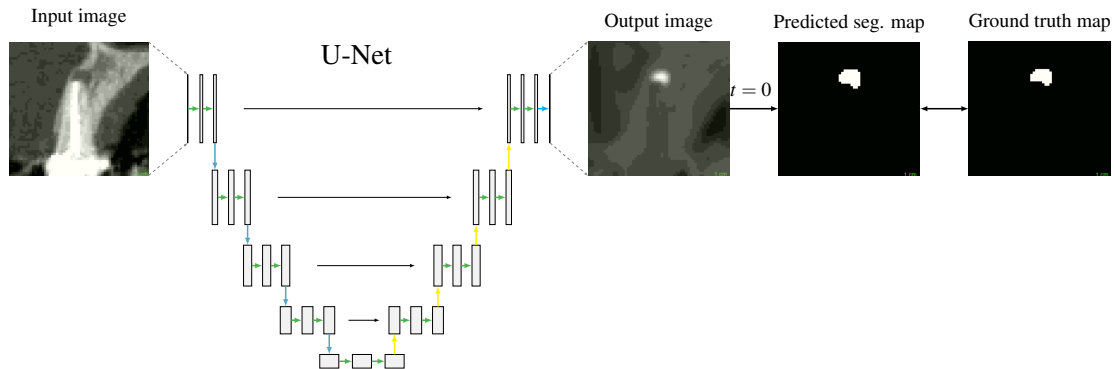


Figure 2: Periapical lesion segmentation using a modified U-Net architecture. A cropped image of a tooth along with its corresponding ground truth map is used as input to the U-Net. The network is trained to output an image of intensity values, where each value lies in the range $(-\infty, +\infty)$. A threshold t is applied to the predicted intensity image in order to generate a final binary segmentation map.

sponds to the center coordinate of a particular tooth. Each cropped image has dimensions of $[64, 64, 64]$ and a spacing of $[0.4, 0.4, 0.4]$. Since periapical osteolytic lesions are always located in the area of the root tips, we translate cropped images by fixed factors to ensure visibility of the entire tooth root within a cropped image. The translation factors of $[0, 1, -9]$ are applied to the cropped images with a tooth in the upper jaw. The cropped images with a tooth in the lower jaw are translated by factors $[0, 3, -9]$ and rotated by 180 degrees. Moreover, all cropped images undergo random translation within the range of $[-1, -1]$, random rotation, and random scaling within the range of $[-0.2, 0.2]$. As a post-processing step, we normalize cropped images to the range $[0, 1]$ and perform shift scale intensity transformation using a random factor of 0.6. We perform label smoothing by applying a Gaussian kernel with a standard deviation of 0.1 to the ground truth segmentation maps.

2.4 Implementation Details

An Intel(R) CPU 920 with an NVIDIA GeForce GTX TITAN X was used for the training and testing of the model. The CNNs were running on Ubuntu 20.04 operating system with Python 3.7 and TensorFlow 1.15.0. To evaluate the performance of our model, we used 4-fold cross validation (cv). Total training time of the SCN for one cv fold took about 20 hours, while one fold for training the U-Net took about 17 hours. The teeth localization network took around 15 seconds for inference on a CBCT volume, while the segmentation network, including cropping, took approximately 2 to 3 minutes.

To minimize the loss function during training of SCN, we use the Nesterov Accelerated Gradient with a learning rate of $10e - 7$ and momentum value of

0.99. We set the number of iterations to 15,000 as we did not observe any substantial improvement after that. Remaining hyper-parameters batch size, weight decay, and sigma regularization term are determined empirically and set to 1, $5e - 5$, and 100, respectively.

The U-Net is trained for 113,000 iterations using a batch size of 8. As mentioned earlier, we address the class imbalance issue by utilizing Focal Loss, Focal Tversky Loss, and Combo Loss. We set the parameters of these loss functions as follows: Within our dataset, positive voxels in each cropped image occupy less than 10% of the volume. Therefore, we set the weighting factors α and β to 0.9 in the corresponding loss functions. The parameter γ controls the down-weighting of easy examples. We set γ to 2 in the Focal Loss and the Focal Tversky Loss function. In the case of the Combo Loss function, we set the parameter δ to 0.5, which determines the contribution of the Balanced Binary Cross-Entropy. Furthermore, in order to minimize the loss functions, we employ the Adam optimizer with a learning rate of $1e - 4$.

Both networks are trained and tested using the 4-fold cross validation technique. For teeth localization, our dataset of 144 3D CBCT images is divided into four cv folds, each containing 36 images. For lesion segmentation, we split a total of 2128 cropped images into four cv folds. Since only 206 teeth in our dataset are affected by a lesion, we distribute them uniformly over all cv folds, resulting in 10% of teeth with lesions and 90% teeth without lesions per fold.

2.5 Metrics

To evaluate the teeth localization performance, we use the point-to-point error (PE) and accuracy metrics. For a landmark i , the point-to-point error PE_i represents the Euclidean distance between the ground

truth landmark \bar{x}_i and the predicted landmark x'_i . Accuracy is defined as the percentage of correctly identified landmarks over all predicted landmarks (i.e., average precision). A predicted landmark x'_i is identified correctly if the closest ground truth landmark is the correct one and the Euclidean distance to the ground truth landmark is less than a specified radius r .

To evaluate the lesion detection performance, we use the metrics sensitivity ($TP/(TP+FN)$) and specificity ($TN/(TN+FP)$). Each predicted segmentation is evaluated based on the Dice score, an overlap measure between the ground truth segmentation map X and the predicted segmentation map Y , defined by

$$DSC = 2 \cdot \frac{|X \cap Y|}{|X| + |Y|}. \quad (9)$$

Sensitivity represents the network’s ability to correctly detect teeth with lesions, whereas specificity represents its ability to correctly detect teeth without lesions. A predicted segmentation map for a tooth with a lesion is classified as a True Positive (TP) if the Dice score between the ground truth and predicted segmentation map is larger than 0. Otherwise, the predicted segmentation map is classified as a False Negative (FN). A predicted segmentation map for a tooth without a lesion is classified as a True Negative (TN) if all voxels in the predicted segmentation map are 0. Otherwise, the predicted segmentation map is classified as a False Positive (FP) prediction.

2.6 Delaunay Triangulation

For the training of the U-Net, each original image is cropped to the size of $[64, 64, 64]$ for each tooth, where the center coordinate of a cropped image corresponds to the center coordinate of the particular tooth in the original image. Since teeth can have different shapes, sizes, and orientations, the resulting cropped images may contain multiple teeth, which complicates automated tooth-based evaluation. To address this issue, we use the definitions of the convex hull and the Delaunay triangulation.

First, we annotate a cuboid around each tooth in the original image using Planmeca Romexis[®] software. This annotation ensures that each cuboid encloses only the area of a single tooth. The software then automatically generates a set of 3D coordinates representing the cuboid. We use these coordinates as input for the ‘Convex-Hull’ and ‘Delaunay’ functions from the SciPy 1.6.2 library. By using the ‘Delaunay.find simplex’ function, we obtain the indices of all the simplices that contain all cuboid voxels. Using these indices, we are able to generate a segmentation map for an annotated cuboid. Finally, during the eval-

uation of a specific tooth, we only consider the voxels that belong to its corresponding annotated cuboid.

3 RESULTS AND DISCUSSION

The results of the teeth localization and lesion segmentation tasks are shown in Table 1 and Table 2, respectively. Moreover, we provide a comparison of the results with SOTA methods for periapical lesion detection in Table 3.

Table 1: Teeth localization results for 4-fold cross validation, showing point-to-point error with standard deviation, as well as accuracy of the model for different radii r .

Radius r	PE in mm Mean \pm SD	Accuracy (%)
2 mm	} 1.74 \pm 1.44	72.6
3 mm		89.1
4 mm		94.7
6 mm		97.3

Table 2: Lesion detection and segmentation results for 4-fold cross validation, shown as sensitivity, specificity, and Dice score obtained using different loss functions.

Loss	Sensitivity	Specificity	DICE
FL	0.97 \pm 0.03	0.88 \pm 0.04	0.67 \pm 0.03
FTL	0.92 \pm 0.05	0.89 \pm 0.08	0.70 \pm 0.04
CL	0.85 \pm 0.04	0.94 \pm 0.02	0.70 \pm 0.04

Table 3: Comparison with SOTA methods.

Method	Sensitivity	Specificity
(Lee et al., 2020)	0.94	-
(Setzer et al., 2020)	0.93	0.88
(Zheng et al., 2020)	0.84	-
(Orhan et al., 2020)	0.93	-
Ours	0.97	0.88

We evaluated the performance of the SCN on 4 folds and achieved an average accuracy of 97.3% in teeth detection, with a mean point-to-point error of 1.74 ± 1.44 mm. In other words, for 97.3% of the predicted teeth, the closest ground truth landmark was the correct one and the distance between the predicted and ground truth landmarks was less than 6 mm. Decreasing the radius to 4, 3, and 2 mm resulted in average accuracy values of 94.7%, 89.1%, and 72.6%, respectively. By observing individual predictions, we could notice that the most incorrect predictions occurred in images affected by artifacts or images with misaligned teeth. This can be attributed to these cases

being rare in our dataset and thus deviating from the learned data distribution. In future work, this could be addressed by combining generative models with CNNs to incorporate global shape/landmark configurations into the training process. This way, the detection of out-of-distribution data could be improved.

The U-Net was trained using the Focal Loss (FL), Focal Tversky Loss (FTL), and Combo Loss (CL) functions. By adjusting the parameters of these loss functions, we were able to reweight the hard and easy class examples. Each setup was evaluated on 4 folds, with uniformly distributed teeth with lesions. The highest lesion detection rate of 0.97 was achieved using FL, whereas FTL and CL achieved the detection rates of 0.92 and 0.88, respectively. The highest specificity value of 0.94 was achieved using CL, while the values of 0.88 and 0.89 were achieved using FL and FTL, respectively. The highest Dice score of 0.70 was achieved using the FTL and CL functions. The setup trained with FL achieved a slightly smaller value of 0.66 for the Dice score. By observing the predictions for individual lesions, we noticed a larger number of false negative predicted voxels and consequently lower Dice scores in images with very small or very large lesions. Small differences between predicted and ground truth segmentation maps have a significant impact on the Dice score for images with very small lesions, while a significant predicted portion of a lesion can result in a low Dice score for images with very large lesions. Since false negative predictions are less tolerable than false positive predictions in the lesion detection task, we conclude that the best performance of our method was achieved using the FL function with a sensitivity value of 0.97 and a specificity value of 0.88. In future work, we plan to explore the use of stronger anatomical constraints via generative models to improve the crucial teeth localization step.

When comparing our method with other SOTA methods, our approach achieved the highest sensitivity value and the same specificity value as (Setzer et al., 2020). However, it is important to note that a direct comparison is not feasible due to the use of different datasets in the evaluation of these methods. Furthermore, all SOTA methods, except (Orhan et al., 2020), utilized 2D slices rather than 3D volumes during the training and testing procedures. Additionally, the studies conducted in (Setzer et al., 2020) and (Zheng et al., 2020) were limited to small respective datasets. When considering the negative class, which refers to teeth without periapical lesions, only (Setzer et al., 2020) reported a specificity value. However, their dataset is highly selective as it consists of only 20 CBCT volumes with limited field-of-view. More-

over, among these volumes, there are 29 roots with lesions and 32 roots without lesions, thus creating a balanced distribution of roots with and without lesions, which does not reflect clinical practice.

4 CONCLUSION

In this paper, we have presented a fully automated two-step method for detecting periapical lesions in CBCT images. In the first step, we utilize the 3D SpatialConfiguration-Net (SCN) for teeth localization. By using the teeth coordinates generated by the SCN, we extract relevant subregions from the original images, and use them to train the 3D U-Net for lesion segmentation in the second step. In contrast to other SOTA methods, our method incorporates 3D volumes throughout all stages, ensuring no loss of valuable information. Additionally, to the best of our knowledge, we are the first to address the class imbalance issue associated with automatic periapical lesion detection, which is commonly observed in clinical data. Despite the challenges posed by dental CBCT images, our method achieved promising results in localizing teeth and detecting periapical lesions in CBCT data.

REFERENCES

- Abraham, N. and Khan, N. M. (2019). A novel focal Tversky loss function with improved Attention U-Net for lesion segmentation. In *2019 IEEE 16th International Symposium on Biomedical Imaging (ISBI 2019)*, pages 683–687. IEEE.
- Antony, D. P., Thomas, T., and Nivedhitha, M. (2020). Two-dimensional periapical, panoramic radiography versus three-dimensional cone-beam computed tomography in the detection of periapical lesion after endodontic treatment: A systematic review. *Cureus*, 12(4).
- Chung, M., Lee, M., Hong, J., Park, S., Lee, J., Lee, J., Yang, I.-H., Lee, J., and Shin, Y.-G. (2020). Pose-aware instance segmentation framework from cone beam ct images for tooth segmentation. *Computers in Biology and Medicine*, 120:103720.
- Cootes, T. F., Hill, A., Taylor, C. J., and Haslam, J. (1994). Use of active shape models for locating structures in medical images. *Image and Vision Computing*, 12(6):355–365.
- Donner, R., Menze, B. H., Bischof, H., and Langs, G. (2013). Global localization of 3d anatomical structures by pre-filtered hough forests and discrete optimization. *Medical Image Analysis*, 17(8):1304–1314.
- Du, M., Wu, X., Ye, Y., Fang, S., Zhang, H., and Chen, M. (2022). A combined approach for accurate and accelerated teeth detection on cone beam ct images. *Diagnostics*, 12(7):1679.

- Ekert, T., Krois, J., Meinhold, L., Elhennawy, K., Emara, R., Golla, T., and Schwendicke, F. (2019). Deep learning for the radiographic detection of apical lesions. *Journal of Endodontics*, 45(7):917–922.
- Endres, M. G., Hillen, F., Salloumis, M., Sedaghat, A. R., Niehues, S. M., Quatela, O., Hanken, H., Smeets, R., Beck-Broichsitter, B., Rendenbach, C., et al. (2020). Development of a deep learning algorithm for periapical disease detection in dental radiographs. *Diagnostics*, 10(6):430.
- Gan, Y., Xia, Z., Xiong, J., Li, G., and Zhao, Q. (2017). Tooth and Alveolar Bone Segmentation From Dental Computed Tomography Images. *IEEE Journal of Biomedical and Health Informatics*, 22(1):196–204.
- He, K., Zhang, X., Ren, S., and Sun, J. (2015). Delving deep into rectifiers: Surpassing human-level performance on ImageNet classification. In *Proceedings of the IEEE International Conference on Computer Vision*, pages 1026–1034.
- Heimann, T. and Meinzer, H.-P. (2009). Statistical shape models for 3D medical image segmentation: A review. *Medical Image Analysis*, 13(4):543–563.
- Jain, A., Tompson, J., Andriluka, M., Taylor, G. W., and Bregler, C. (2014). Learning human pose estimation features with convolutional networks. In *2nd International Conference on Learning Representations (ICLR)*, pages 1–11.
- Khanagar, S. B., Al-Ehaideb, A., Vishwanathaiah, S., Maganur, P. C., Patil, S., Naik, S., Baeshen, H. A., and Sarode, S. S. (2021). Scope and performance of artificial intelligence technology in orthodontic diagnosis, treatment planning, and clinical decision-making—a systematic review. *Journal of Dental Sciences*, 16(1):482–492.
- Kirnbauer, B., Hadzic, A., Jakse, N., Bischof, H., and Stern, D. (2022). Automatic detection of periapical osteolytic lesions on cone-beam computed tomography using deep convolutional neuronal networks. *Journal of Endodontics*, 48(11):1434–1440.
- Krois, J., Garcia Cantu, A., Chaurasia, A., Patil, R., Chaudhari, P. K., Gaudin, R., Gehrung, S., and Schwendicke, F. (2021). Generalizability of deep learning models for dental image analysis. *Scientific Reports*, 11(1):6102.
- Lee, J.-H., Kim, D.-H., and Jeong, S.-N. (2020). Diagnosis of cystic lesions using panoramic and cone beam computed tomographic images based on deep learning neural network. *Oral Diseases*, 26(1):152–158.
- Lin, T., Goyal, P., Girshick, R. B., He, K., and Dollár, P. (2017). Focal loss for dense object detection. In *IEEE International Conference on Computer Vision*, pages 2999–3007. IEEE.
- Orhan, K., Bayrakdar, I., Ezhov, M., Kravtsov, A., and Özyürek, T. (2020). Evaluation of artificial intelligence for detecting periapical pathosis on cone-beam computed tomography scans. *International Endodontic Journal*, 53(5):680–689.
- Pauwels, R., Brasil, D. M., Yamasaki, M. C., Jacobs, R., Bosmans, H., Freitas, D. Q., and Haiter-Neto, F. (2021). Artificial intelligence for detection of periapical lesions on intraoral radiographs: Comparison between convolutional neural networks and human observers. *Oral Surgery, Oral Medicine, Oral Pathology and Oral Radiology*, 131(5):610–616.
- Payer, C., Stern, D., Bischof, H., and Urschler, M. (2019). Integrating spatial configuration into heatmap regression based CNNs for landmark localization. *Medical Image Analysis*, 54:207–219.
- Payer, C., Stern, D., Bischof, H., and Urschler, M. (2020). Coarse to fine vertebrae localization and segmentation with SpatialConfiguration-Net and U-Net. In *VISIGRAPP (5: VISAPP)*, pages 124–133.
- Ronneberger, O., Fischer, P., and Brox, T. (2015). U-net: Convolutional networks for biomedical image segmentation. In *Medical Image Computing and Computer-Assisted Intervention – MICCAI 2015*, pages 234–241. Springer International Publishing.
- Setzer, F. C., Shi, K. J., Zhang, Z., Yan, H., Yoon, H., Mupparapu, M., and Li, J. (2020). Artificial intelligence for the computer-aided detection of periapical lesions in cone-beam computed tomographic images. *Journal of Endodontics*, 46(7):987–993.
- Taghanaki, S. A., Zheng, Y., Zhou, S. K., Georgescu, B., Sharma, P., Xu, D., Comaniciu, D., and Hamarneh, G. (2019). Combo loss: Handling input and output imbalance in multi-organ segmentation. *Computerized Medical Imaging and Graphics*, 75:24–33.
- Umer, F. and Habib, S. (2022). Critical analysis of artificial intelligence in endodontics: a scoping review. *Journal of Endodontics*, 48(2):152–160.
- Unterpinker, W., Ebner, T., Štern, D., and Urschler, M. (2015). Automatic third molar localization from 3D MRI using random regression forests. In *19th International Conference on Medical Image Understanding and Analysis (MIUA)*, pages 195–200, Lincoln, UK.
- Urschler, M., Ebner, T., and Štern, D. (2018). Integrating geometric configuration and appearance information into a unified framework for anatomical landmark localization. *Medical Image Analysis*, 43:23–36.
- Urschler, M., Leitinger, G., and Pock, T. (2014). Interactive 2D/3D image denoising and segmentation tool for medical applications. In *Proceedings MICCAI Workshop Interactive Medical Image Computation (IMIC)*.
- Yushkevich, P. A., Piven, J., Cody Hazlett, H., Gimpel Smith, R., Ho, S., Gee, J. C., and Gerig, G. (2006). User-guided 3D active contour segmentation of anatomical structures: Significantly improved efficiency and reliability. *Neuroimage*, 31(3):1116–1128.
- Zhang, J., Liu, M., and Shen, D. (2017). Detecting anatomical landmarks from limited medical imaging data using two-stage task-oriented deep neural networks. *IEEE Transactions on Image Processing*, 26(10):4753–4764.
- Zheng, Z., Yan, H., Setzer, F. C., Shi, K. J., Mupparapu, M., and Li, J. (2020). Anatomically constrained deep learning for automating dental cbct segmentation and lesion detection. *IEEE Transactions on Automation Science and Engineering*, 18(2):603–614.